3D Particle Tracking Velocimetry applied to bubble plumes from a free falling jet

R.G. Ramirez de la Torre[1*], Miroslav Kuchta[2], Atle Jensen[1]

[1] University of Oslo, Department of Mathematics, Oslo, Norway

[2] Simula Research Laboratory, Fornebu, Norway

[*] reynar@math.uio.no

Abstract

The focus of the present study was the behaviour of a bubble plume created by a circular free falling jet. The objective was to find a relation between the disturbances on the jet surface and the air entrainment process. To achieve this, the instabilities of the free falling jet were characterized and compared with the size distribution and generation rate of the bubbles created in the plume. The bubble trajectories were obtained and used to determine the jet-pool interaction after the impact.

1 Introduction

In the atmosphere and within the marine boundary layer the interaction between air and water is constant and takes different forms. In case of the phenomena involving droplets or bubbles, there is a large number of challenges: the three-dimensionality of the phenomena, the highly turbulent regions, the wide distributions of sizes in both droplets and bubbles, to name but a few. An important example of this difficult phenomena is ocean spray in artic sea freezing on top of vessels. Understanding of this phenomena is important for the safety of installations, ships and people that operate in the Arctic environment. The icing phenomena and its consequences have been documented for several years (see e.g. Ryerson (2013)). Some references report that the major causes of icing are the sea spray and the atmospheric conditions (Bodaghkhani et al., 2016). The sea spray formation is caused by wave impact and wind. According to Borisenkov and Pchelko (1975) more than 90% of the icing is caused by the spray that comes from wave impact. It has been reported that the physical behaviour of wave impact is not properly understood. Furthermore, the multi-scale nature, complexity of spray and icing require that the research on this field is separated into smaller problems, such as the modelling of the free-surface, wave slamming, air entrainment during the impact, water sheet and jet formation during the wave slamming, water sheet and droplet breaking caused by wind and droplet trajectories before they impact on the surface of ships or structures (Bodaghkhani et al., 2016; Dommermuth et al., 2007).

The ambition of spray and icing research is to generate models that are able to predict the amount of icing on a structure from ocean spray. Here, we focused on experiments to bring understanding of the spray and bubble plume phenomena, in particular, the size distributions, which are not well known and are an important input for simulations of breaking waves on naval structures. A simplified system, which however, is still complex enough to capture the difficulty of measuring sea spray and air entrainment is the circular falling jet. For the case of bubble generation in falling jets, the ratio of entrained air and the size distribution of the bubbles has been estimated using conductivity probes, resistivity probes and acoustic probes (Chanson et al., 2006; Wang et al., 2016; Deane, 1997; Kolaini, 1998). All of these probes have been used with positive outcomes but the characteristics of the observed phenomena also show the limitations of the applied techniques. These probes are invasive methods and the data obtained is only for a particular point in the domain. For highly turbulent flows these techniques are non-adequate, except maybe the acoustic probes. Moreover, the resistivity and conductivity probes are dependent on the size of the instrumentation, i.e. different probe sizes can give different measurements for the same parameters on the jet (Chanson et al., 2006). This is not the case for the acoustic probes, nonetheless these types of probes can only approximate the void fraction and not the size distribution.

(a) Diagram of full experimental setup.

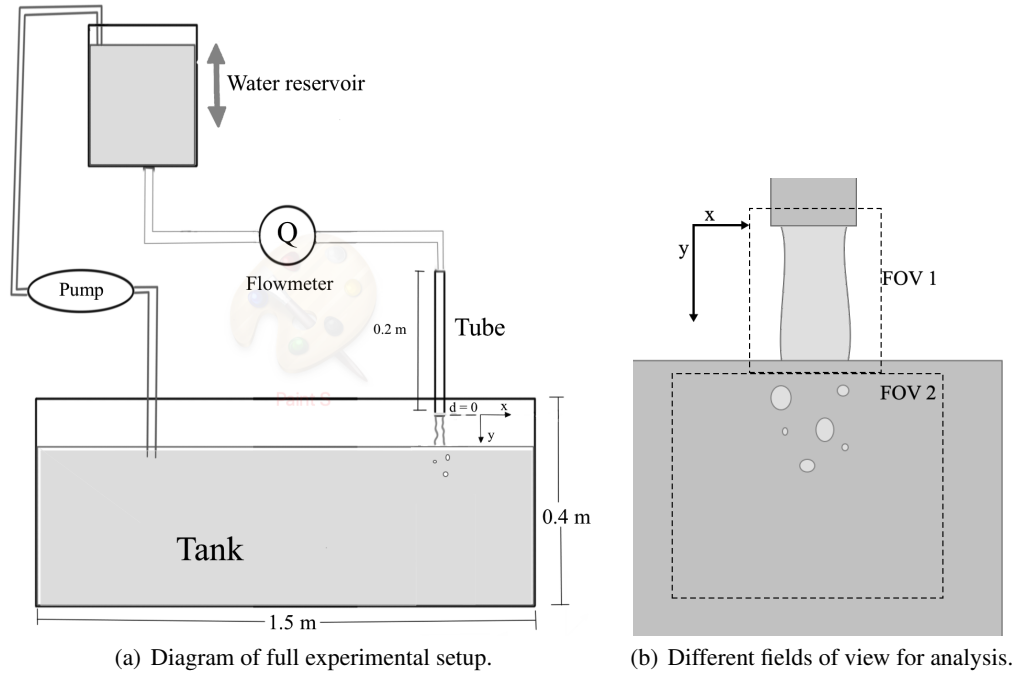(b) Different fields of view for analysis.

Figure 1: Experimental Setup.

Imaging methods can in some cases be used for measuring droplets and bubbles. By using images, it is possible to capture the complete domain, in contrast to the point-wise measurements obtained by the probes. Post processing of these images is commonly done with Particle Image Velocimetry (PIV) or Particle Tracking Velocimetry (PTV). The usage of one of these algorithms is determined by the type of analysis that is desired. PIV measurements are commonly used to track the fluid movements from an Eulerian approach, PTV measurements are used to obtain a Lagrangian description. For PTV, using more than one camera at the same time can result in 3D reconstruction of the trajectories of the particles and their velocities. The advantage of this kind of algorithms is that they consider the camera parameters to estimate the positions of the blurry particles present in the images and with the correlation of the images from the different cameras, reduce the error on the positions for each particle in each time step.

In this work imaging techniques and a 3D-PTV algorithm were used to understand the parameters involved in the air entrainment produced by a circular falling jet. The experiments involved the study of different parts of the process: formation and development of disturbances in the surface of the jet, identification of the conditions under which the entrainment occurs and finally the formation of bubbles and its characteristics. The experimental setup and the different approaches and measuring techniques needed to understand each part are described in section 2. We present and analyze the obtained results in section 3. Conclusions are drawn in section 4.

2 Experimental Description

The experiments were conducted in a small tank with dimensions $1.50 \text{ m} \times 0.40 \text{ m} \times 0.40 \text{ m}$, as shown in Figure 1. Water was stored in a 10 litre reservoir, then went down through a hose towards the tank. In the middle of its path, there was a flowmeter, from which the flux or flow rate (Q) was obtained. Before falling down to the tank, the water went through the exit pipe, which was a 20 cm long plastic tube. The tube was fixed such as to ensure a perpendicular fall of the jet. To create the different falling speeds, the reservoir was moved in the vertical direction. The water was also recycled with the help of a pump. The pump was off during the measurements to avoid undesired effects.
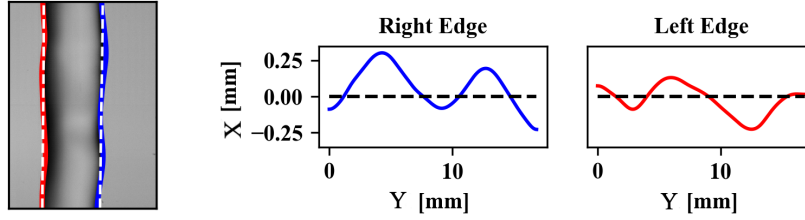
(a) Jet image and edge detection, the dashed white line represents the zero crossing.

(b) Graphs of edges in data shape.

Figure 2: Edge extraction process.

2.1 Jet disturbances and the entrainment process

For the jet disturbances, the images were obtained with a Photron FASTCAM SA5 camera. The frame rate was 500 FPS with $1/2000$ ms of shutter speed. The image resolution was 640×1024 pixels. The Field of View (FOV) was approximately 2 cm height, see Figure 1(b). The illumination was provided by LED lamps. The light was diffused with white plastic sheets and difusser sheets. As the disturbances presented in the surface were non-controlled, it was expected for them to have random behaviour. Therefore, careful record of the amplitude a, wavelength λ, and frequency f of the disturbances was made and the jet disturbances were analyzed as surface waves. As shown in Figure 2, the edges of the jet were extracted from the images and collected in a space-temporal array: $x(y,t)$. A mean level was defined by averaging the data set in time $\xi(y) = \overline{x(y,t)}$. Then, the wave height was obtained by subtracting the mean level: $\eta(x,t) = x(y,t) - \xi(y)$. A wavelength ($\lambda$) in η was define as the length from through to trough and the amplitude (a) of the wave was defined as the height of the crest between the throughs.

For each falling distance d we had a range of Q's. For each Q, we obtained an outlet velocity (V_{out}) and estimated a falling velocity at the confluence point (V_{jet}) with the equations

$$V_{jet} = \sqrt{V_{out}^2 + 2gd}, \quad V_{out} = \frac{Q}{A}, \tag{1}$$

where A is the cross section area of the tube and g is gravity acceleration. From these velocities we also obtained Reynolds numbers for the outlet flux (Re_{out}) and estimated a Reynolds number for the falling jet (Re_{jet}). In general, the Reynolds number is defined as

$$Re = \frac{VD}{\nu}, \tag{2}$$

where D is the diameter of the correspondent flow, for Re_{out}, $D = D_{out}$, the diameter of the tube and for Re_{jet}, $D = D_{jet}$, the diameter of jet at the confluence point, and ν is the dynamic viscosity of water.

For the entrainment process, a set up of synchronized cameras was used to capture simultaneous images of the jet and the entrainment underwater. Two AOS Promon U1000Mono cameras were used. These cameras were synchronized at 500 FPS, with $1/500$ ms shutter, with resolution 608×800 pixels. Both FOV's were around 2-3cm height. The FOV of the first camera was centered at the jet falling while the other camera's FOV was centered in the confluence area under the pool surface.The recordings were 20 seconds long. The illumination was provided in the same way as in the previous case. These synchronized image sequences had as main objective the visualisation of the entrainment process in a qualitative way. Also, the underwater images were used to obtain a number of produced bubbles for each Q and each d.

2.2 Bubbles characteristics

For the tracking of bubbles, a group of 4 AOS Promon U1000Mono cameras was used. The cameras were synchronised with a frame rate of 350 FPS, $1/500$ ms shutter and an image resolution of 1280×720 pixels.
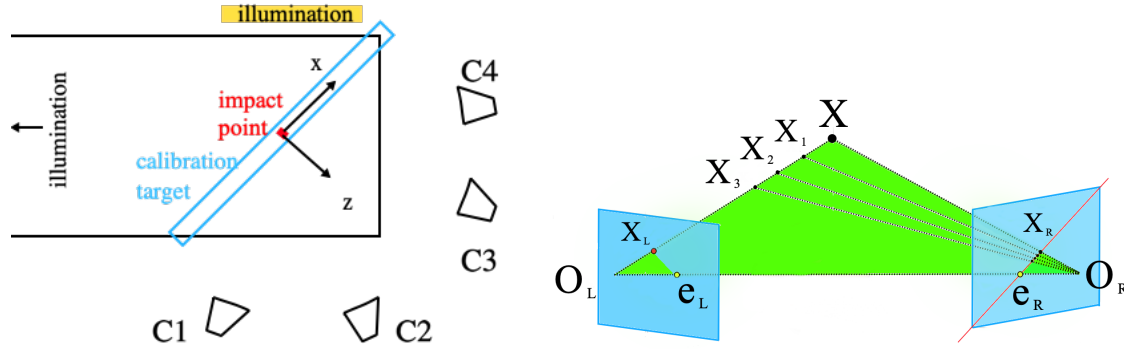
(a) Diagram of the cameras setup for 3D PTV. C1-C4 shows the position of the cameras compared to the tank. The diagram shows also the calibration target in blue. The outlet of the tube to the surface of the water is pinpointed with the red dot.

(b) Diagram of algorithm to reconstruct 3D trajectories with epipolar lines. Points O_L and O_R represent the centers of each camera lens, while X represents an arbitrary particle. X_L and X_R are the projections of X in the respective image plane. Each camera center is also visible in each others image plane. These so called epipolar points are depicted by points e_L and e_R. The line $\overline{O_L X}$ is seen as a point in the left camera, whereas the same line is seen as an epipolar line $\overline{e_R X_R}$ in the image plane of right camera. The same applies to line $O_R X$ which is seen as a point in the right camera and as an epipolar line in the left camera's image plane.

Figure 3: PTV Camera setup and description of the 3D position algorithm.

The illumination was provided by a similar setup as in the previous cases. The cameras were arranged in a stereoscopic setup for the reconstruction of the 3D positions of the bubbles, cf. Figure 3(b). The FOV is approximately 12 cm height and is below the area of analysis used in the previous setups where the plume is totally developed.

OpenPTV software was used to reconstruct the 3D positions and trajectories of the bubbles. OpenPTV uses image processing to detect particles in the images. Then using the method described in Maas et al. (1993), finds the correspondences in the 4 images, in this way the three dimensional positions are reconstructed for each time step.

PTV method represents the Lagrangian approach to investigate flows. To obtain three dimensional trajectories, the particles need to be matched among all views. The method used by OpenPTV finds correspondences based on epipolar geometry. Figure 3(b) depicts the definition of an epipolar line with two cameras. Since the line $\overline{O_L X}$ passes through the optical center of lens O_L, the respective epipolar line in the right image must pass through the epipolar point regardless of where point X is located. In OpenPTV the relative position of the cameras system are known from a previous and very careful calibration. When a particle is observed in one image, the same particle has to be observed on a known epipolar line in the other image. Furthermore, if points X_L and X_R are known, their projection lines $\overline{O_L X}$ and $\overline{O_R X}$ are also known. Consequently, point X is located exactly at the intersection of the two projection lines and thus can be calculated from the image coordinates of the two images. This figure illustrates the need for a good calibration for three-dimensional particle tracking.

The next processing stage is to compare particles in consecutive time steps and determine their trajectories. The length of the trajectories is dependant on the position, the size and the acceleration of the particle. Tracking can be especially difficult with a large number of particles present. According to Malik et al. (1993) the particle spacing displacement ratio p is a fundamental indicator on the difficulty to track particles with this method. The ratio is defined as

$$p = \frac{\Delta O}{u \Delta t} \tag{3}$$

with ΔO the mean particle spacing, u the mean velocity of the particles and Δt the time step between images. For $p > 1$ tracking is reliable, while for $p < 1$ tracking becomes difficult. In other words, the farther particles are from each other and the slower they move, the more reliable the method is. OpenPTV uses a spatio-temporal tracking algorithm which is described in Maas et al. (1993) and Willneff (2003). As input, this algorithm needs eight parameters. These include the minimum and maximum displacement in

$d[m]$	Re	We
0.02	6100-9000	1-137
0.04	7200-9700	9-155
0.06	8100-10400	5-158

Table 1: Relevant nondimensional parameters for each falling distance d

each coordinate direction, the angle of the particle in the direction along its trajectory and a magnitude of acceleration. Since these parameters constitute the boundary conditions of the particle velocities, it is important to have an estimate of the expected velocities. After obtaining the correspondences and the trajectories, custom made Python codes were used to analyze the data obtained, plot the trajectories and obtain the velocity fields.

A range of Weber number (We) can be obtained from the bubble size distribution. We was defined as

$$We = \frac{\rho V_{jet}^2 D_b}{\sigma},\qquad(4)$$

where ρ is water density, D_b is the bubble diameter and σ is the surface tension for air and water. Weber number is an important parameter on the interaction of the bubble with the media. It expresses the ratio between the inertial forces and the surface tension and it is the relevant parameter to describe the deformation of the bubbles. Therefore is important to describe their possible trajectory and the coalesence probability. For bubbles that present low deformation, Weber number has values of $O(2)$ (Legendre et al., 2012). If we consider the bubbles to be spheroids, with axes a and b, $We > 10$ would signify a ratio $a/b > 4$. Reynolds and Weber number for the different experiments made can be found in Table 1.

3   Results

The air entrainment process has been studied in numerous works and for different geometries (Kiger and Duncan, 2012; Zhu et al., 2000). The conditions of its development have been shown to be dependant on a large number of parameters. Therefore it keeps being interesting to find the different dependencies of this problem. In this study, the focus was to understand the formation of air pockets due to the disturbances that appear on the surface of a circular falling jet and the dynamics of the bubble plume formed after the air entrainment. We shall next describe the most important findings.

3.1   Jet disturbances and entrainment process

A great amount of work has been done to understand the air entrainment process (Kiger and Duncan, 2012; Zhu et al., 2000; Soh et al., 2005; Chanson et al., 2004), the synchronised surface-underwater images are qualitative evidence of the conditions of the phenomena. In Figure 4 it is possible to follow the impingement of two different disturbances in to the pool. The main difference between these disturbances is that the first (closest to the pool, Fig.4(a)) has longer wavelength compared to the second. In other words, the first disturbance has smaller steepness than the second one. It is clear that the first disturbance impinges the pool and enters without the generation of any air pocket or any significant change in the pool surface (Fig. 4(a)-4(c)). Subsequently, the second disturbance approaches the pool surface and impinges on it. After the impingement an air pocket is created and it is pulled down by the jet velocity (Fig. 4(d)-4(g)). The finger finally breaks to form a bubble that will continue travelling underwater pulled by the jet. This is a clear example of a typical entrainment occurrence in the experiments developed for this study. The image sequence is comparable to the sketches presented in Kiger and Duncan (2012) and Zhu et al. (2000) for disturbances with large amplitude. In this study we put forward a hypothesis that the steepness of the disturbance is possibly more significant than the amplitude. This hypothesis can be supported by Figure 4, where two disturbances with comparable amplitude produced different effects on the pool and the disturbance with considerably smaller wavelength was the only one that produced entrainment. This possible dependency should be further studied.
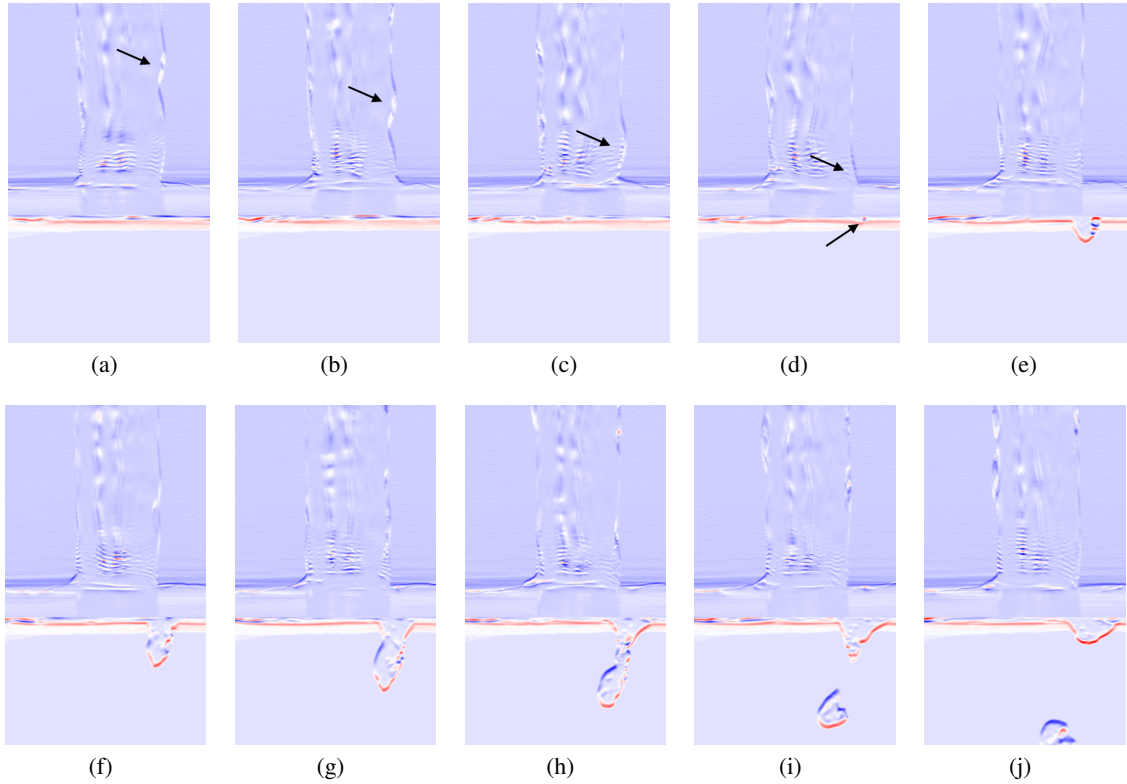
Figure 4: Sequence of images that shows the entrainment process for a steep disturbance in the jet. The diameter of the jet at the impingement point is approximately 5mm. Sobel derivatives were used to enhance the edges of the interfaces. (a) Two waves are visible, the top one with larger steepness (pointed with the arrow), this is the wave to follow. (b) The first wave enters, there is no air entrainment. (c) The second wave approaches. (d) The second wave enters the pool, air entrainment begins. (e) The formation of the air finger is visible while the jet pulls it down. (f) The air finger grows. (g) The air finger continues growing. (h) The finger break up starts caused by the speed of the jet. (i) The finger finally breaks and a bubble is created. (j) The cavity from the finger closes and the surface starts contracting upwards again.

In addition to the raw entrainment of air in to the pool, it is also interesting to turn our eyes to the formation of bubbles after the air pockets broke. For the different d there is a different span of Reynolds numbers that we showed in Table 1. From the results of the experiments, it is possible to say that the air entrainment has a Reynolds onset value close to 8000. These results are summarized in Figure 5. Although for large d it is also noticeable that the number of bubbles is reduced. This can actually be explained by inspecting the images of the entrainment. The air pockets produced by greater Reynolds are also larger in size which reduces the count of bubbles. The bubbles visible in this setup will have greater size and eventually will break into smaller ones, leaving behind a very dense bubble plume that will be visible in the next step of the analysis.

3.2 Bubble characteristics

The bubble plume under a falling jet is an interesting phenomena to observe. It is a case of multiphase flow where many parameters can be considered especially when the number and sizes of the bubbles are also dependant on the velocity of the falling jet. These bubbles are not only tracers of the present flow but also a consequence of it. However reliable measurements of this plume become difficult when the density of bubbles and range of sizes is high. In this section we present the results of an attempt to extract information from different plume conditions and the advantages and limitations of the 3D PTV technique used to perform the analysis.

In Figure 6(a) the index p, presented in equation 3, is shown for all different analyzed cases. Although
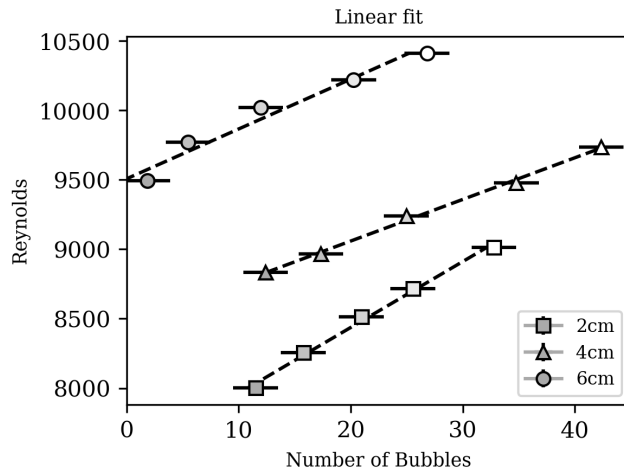
Figure 5: Reynolds of the falling jet against number of bubbles. The graph shows the estimated Reynolds number of the falling jet when impinging in the pool and compares it with the mean number of bubbles visible in the image sequence. It is visible that the amount of bubbles is directly proportional to the Reynolds number. The fitted lines are $0.028(05)x - 265(5)$ for d=2 cm, $0.021(05)x - 157(5)$ for d=4 cm, $0.033(05)x - 282(5)$ for d=6 cm.
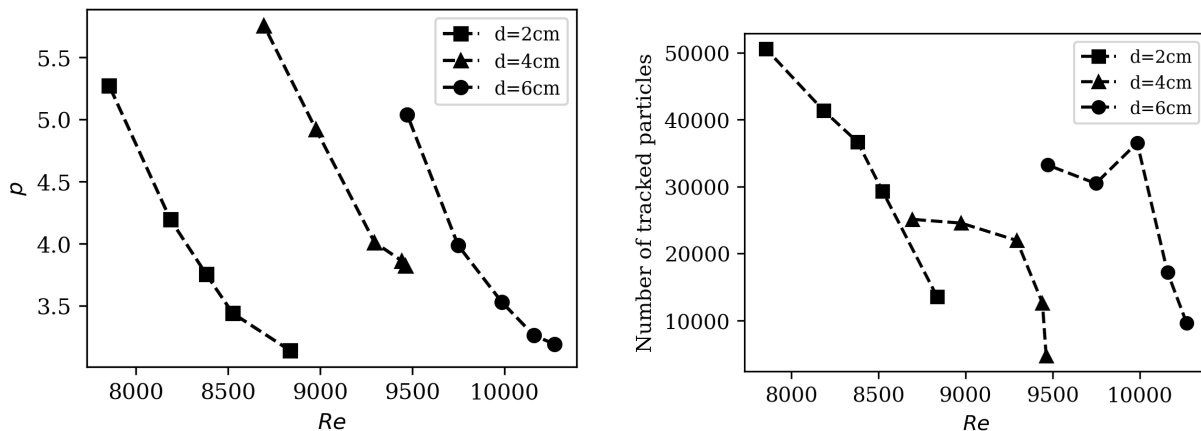
(a) Different values of p for all the cases analyzed in this study. We compare with the velocity of the jet in the impingement point and we see the difference for the falling distances.

(b) Total number of particles tracked in at least two consecutive frames compares with the Reynolds number of the jet.

Figure 6: Graph of different values of p and total particles tracked in at least two consecutive frames

(a) Bubbles 3D positions. The colour represents the instant velocity in the vertical direction, red points indicate bubbles moving downwards and blue points indicate bubbles moving upwards.

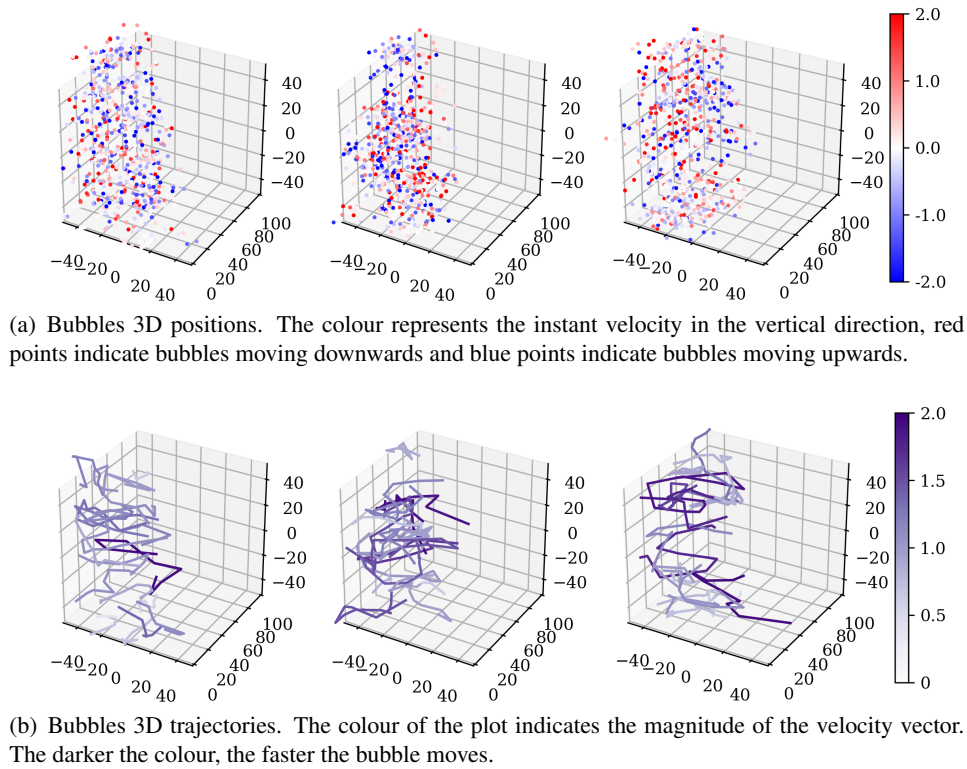(b) Bubbles 3D trajectories. The colour of the plot indicates the magnitude of the velocity vector. The darker the colour, the faster the bubble moves.

Figure 7: Results of 3DPTV tracking

in all cases $p > 1$, it is only in a few cases where $p > 5$, the value for which mislinks reduce considerably according to Malik et al. (1993). This means that the bubbles can be tracked but with certain difficulty. Therefore, it is important to use carefully the parameters needed to track the particles during the procedure. In Figure 6(b), the efficiency of the tracking algorithm is shown. For this type of dense plume, the amount of particles that can be traced to the next step decreases with increasing Reynolds. Surprisingly, the amount of bubbles that can be followed for more than 10 times steps seems to increase with the Reynolds number, as it is shown in Table 2.

The trajectories of the bubbles and their velocities can be found in Figure 7 . From left to right results for the different falling distances d are presented. No distinguishable difference can be seen in the velocity fields shown in Figure 7(a). For all the cases there are bubbles moving upwards and downwards with considerable high velocity. Perhaps a separation of the bubble velocities depending on the bubble size could give a certain trend for the different d and Re. From Figure 7(b) it is possible to observe that the movement of the bubbles is also great in the horizontal plane. This is expected as the common trajectories for the bubbles are helicoidal, specially when the bubbles have considerable big diameter. This behaviour is probably enhanced by the jet velocity. It is important to mention that the total length of the bubbles plume is not visible in the analysis therefore no conclusion can be obtained on the length of the plume from this analysis.

In Figure 8 some probability distributions are shown for the higher Re in each distance. In Figure 8(a) the distribution of the bubbles around the center of the jet is shown while Figure 8(b) shows the distribution of vertical velocities. Bubbles that move downwards have negative velocity while bubbles that move upwards have positive velocity. In Figure 8(c) typical size distribution are presented. No remarkable differences are visible in the distributions.
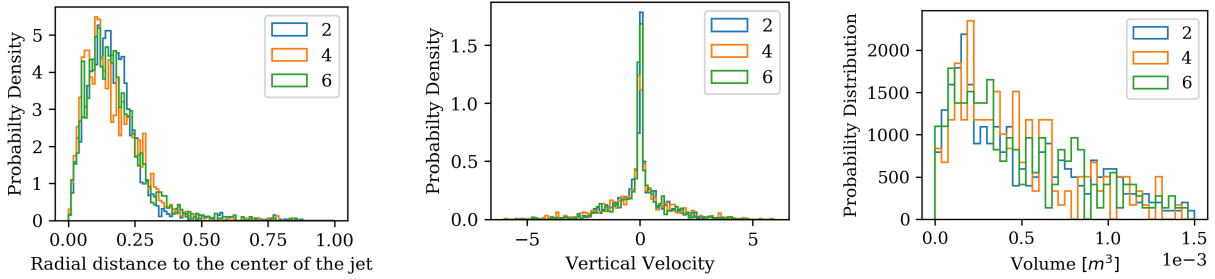
(a) Position to the center of the jet. The x axis represents the distance r/l where r is the distance of the bubble to center and l is the total FOV length.

(b) Vertical velocities of the bubbles in the plume for different falling distance.

(c) Size Distribution of Bubbles in the plume for different falling distance.

Figure 8: Different Distributions

d = 0.02 m	Re	7854	8186	8381	8524	8837
	%	5	7	6	6	11
d = 0.04 m	Re	8694	8975	9294	9441	9462
	%	5	6	6	8	27
d = 0.06 m	Re	9471	9747	9985	10159	10269
	%	5	6	1	11	10

Table 2: Comparison of the Reynolds number with the percentage of particles that are tracked for at least 10 frames. The data from the different jet lengths d is shown.

4   Conclusions

In this work a bubble plume created by a circular free falling jet was studied by means of imaging techniques. From image sequences of the air entrainment process qualitative relations between the jet characteristics and the bubbles created were found. Further, a linear trend was obtained when comparing the Reynolds number and the bubble count. The trajectories of the bubbles were reconstructed, in spite of the variability of the sizes.

The results presented are promising for further analysis. In the future we aim to improve the tracking by addressing in a robust manner the case of bubble break up into two or more bubbles. Such tools could then be applied to study dynamics of the jet after the impact, in particular, for reliable reconstruction of bubble trajectories.

Acknowledgements

References

Bodaghkhani A, Dehghani SR, Muzychka YS, and Colbourne B (2016) Understanding spray cloud formation by wave impact on marine objects. *Cold Regions Science and Technology* 129:114–136

Borisenkov YP and Pchelko I (1975) Indicators for forecasting ship icing. Technical report

Chanson H, Aoki S, and Hoque A (2006) Bubble entrainment and dispersion in plunging jet flows: fresh-water vs. seawater. *Journal of Coastal Research* pages 664–677

Chanson H, Aoki Si, and Hoque A (2004) Physical modelling and similitude of air bubble entrainment at vertical circular plunging jets. *Chemical engineering science* 59:747–758

Deane GB (1997) Sound generation and air entrainment by breaking waves in the surf zone. *The journal of the acoustical society of America* 102:2671–2689

Dommermuth DG, O'Shea TT, Wyatt DC, Ratcliffe T, Weymouth GD, Hendrikson KL, Yue DK, Sussman M, Adams P, and Valenciano M (2007) An application of cartesian-grid and volume-of-fluid methods to numerical ship hydrodynamics. Technical report. SCIENCE APPLICATIONS INTERNATIONAL CORP SAN DIEGO CA

Kiger KT and Duncan JH (2012) Air-entrainment mechanisms in plunging jets and breaking waves. *Annual Review of Fluid Mechanics* 44:563–596

Kolaini AR (1998) Sound radiation by various types of laboratory breaking waves in fresh and salt water. *The Journal of the Acoustical Society of America* 103:300–308

Legendre D, Zenit R, and Velez-Cordero JR (2012) On the deformation of gas bubbles in liquids. *Physics of Fluids* 24:043303

Maas H, Gruen A, and Papantoniou D (1993) Particle tracking velocimetry in three-dimensional flows. *Experiments in fluids* 15:133–146

Malik N, Dracos T, and Papantoniou D (1993) Particle tracking velocimetry in three-dimensional flows. *Experiments in Fluids* 15:279–294

Ryerson CC (2013) Icing management for coast guard assets. Technical report. ENGINEER RESEARCH AND DEVELOPMENT CENTER HANOVER NH COLD REGIONS RESEARCH

Soh WK, Khoo BC, and Yuen WD (2005) The entrainment of air by water jet impinging on a free surface. *Experiments in fluids* 39:498–506

Wang H, Bertola N, and Chanson H (2016) Bubble entrainment in vertical plunging jets

Willneff J (2003) *A spatio-temporal matching algorithm for 3D particle tracking velocimetry*. Ph.D. thesis. ETH Zurich

Zhu Y, OĞUZ HN, and Prosperetti A (2000) On the mechanism of air entrainment by liquid jets at a free surface. *Journal of Fluid Mechanics* 404:151–177